CrossMark

ORIGINAL PAPER

Experimental determination of quartz solubility and melting in the system SiO$_2$–H$_2$O–NaCl at 15–20 kbar and 900–1100 °C: implications for silica polymerization and the formation of supercritical fluids

Miguel F. Cruz[1,2] · **Craig E. Manning**[1]

Abstract We investigated quartz solubility and melting in the system SiO$_2$–NaCl–H$_2$O at 15–20 kbar and 900–1100 °C using hydrothermal piston–cylinder methods. The solubility of natural, high-purity quartz was determined by weight loss. Quartz solubility decreases with increasing NaCl mole fraction (X_{NaCl}) at fixed pressure and temperature. The decline is greatest at low X_{NaCl}. The solubility patterns can be explained by changes in the concentration and identity of silica oligomers. Modeling of results at 1000 °C, 15 kbar, reveals that silica monomers and dimers predominate at low Si concentration (high X_{NaCl}), that higher oligomers assumed to be trimers become detectable at $X_{NaCl} = 0.23$, and that the trimers contain >50 % of dissolved Si at $X_{NaCl} = 0$. The modeling further implies a hydration number for the silica monomer of 1.6, significantly lower than is observed in previous studies. Results at 15 kbar and 1100 °C provide evidence of two coexisting fluid phases. Although solubility could not be determined directly in these cases, the presence or absence of phases over a range of bulk compositions permitted mapping of the topology of the phase diagram. At 1100 °C, 15 kbar, addition of only a small amount of NaCl ($X_{NaCl} = 0.05$) leads to separation of two fluid phases, one rich in H$_2$O and SiO$_2$, the other rich in NaCl with lower SiO$_2$. Textural identification of two fluids is supported by very low quench pH due to preferential partitioning of Na into the fluid that is rich in SiO$_2$ and H$_2$O, confirmed by electron microprobe analyses. The addition of NaCl causes the upper critical end point on the SiO$_2$–H$_2$O melting curve to migrate to significantly higher pressure. Correspondence between depolymerization and phase separation of SiO$_2$–H$_2$O–NaCl fluids indicates that polymerization plays a fundamental role in producing critical mixing behavior in silicate–fluid systems.

Keywords Quartz solubility · Quartz melting · Supercritical fluids · Brines · Experimental petrology

✉ Miguel F. Cruz
  mfcruz@stanford.edu

1 Department of Earth, Planetary and Space Sciences, University of California Los Angeles, Los Angeles, CA 90095, USA

2 Present Address: Geological and Environmental Sciences, Stanford University, Stanford, CA 94305, USA

Introduction

Silica is the major rock-forming component of the crust and mantle, so its interaction with aqueous fluids is important to wide range of metamorphic and igneous processes. In the system SiO$_2$–H$_2$O, quartz solubility increases with pressure (*P*) and temperature (*T*), reaching ~10 wt% at the conditions of the deep crust and upper mantle (Kennedy et al. 1962; Anderson and Burnham 1965; Manning 1994; Zotov and Keppler 2002; Hudon et al. 2002; Newton and Manning 2008; Hunt and Manning 2012). The interaction between H$_2$O and SiO$_2$ also exerts a major control on the melting behavior of silicate rocks. For example at 7 kbar, the dry melting temperature of quartz is ~1700 °C (Jackson 1976; Hudon et al. 2002), whereas hydrous melting in the system SiO$_2$–H$_2$O occurs at 1075 °C and the solubility of H$_2$O in the liquid exceeds 10 wt% (Kennedy et al. 1962). The large mutual solubilities of SiO$_2$ in H$_2$O and H$_2$O in SiO$_2$ lead to full miscibility in the system SiO$_2$–H$_2$O at relatively low *T* at a given *P*, such that the hydrous melting/solubility curve terminates in two critical end points. The higher *T*, or upper, critical end point lies at ~9.8 kbar

and ~1080 °C (Kennedy et al. 1962; Newton and Manning 2008; Hunt and Manning, 2012). Critical mixing of silicate liquid and H_2O is important for fluid–rock phase relations in a wide range of bulk compositions (Paillat et al. 1992; Shen and Keppler 1997; Bureau and Keppler 1999; Stalder et al. 2000, 2001; Mibe et al. 2004; Manning 2004; Hermann and Spandler 2008; Hermann et al. 2006, 2013; Hack et al. 2007a, b; Zheng et al. 2011; Mibe et al. 2007, 2011; Kawamoto et al. 2012).

Although studies of systems in which H_2O is the only solvent component are useful guides to fluid–rock interaction in high-P environments, it is also necessary to consider the effects of additional fluid components. Carbon (e.g., as CO_2) may be abundant in lower-crustal and upper-mantle fluids. In the system SiO_2–H_2O–CO_2, increasing CO_2 mole fraction leads to decreasing quartz solubility at a given P and T (e.g., Walther and Orville 1983; Newton and Manning 2000; Shmulovich et al. 2001, 2006), and increasing T of melting at a given P (Boettcher 1984). The combination of lower solubility and higher melting T at fixed CO_2 mole fraction suppresses critical mixing of SiO_2 and fluid by increasing the size of the liquid + vapor miscibility gap, and by pushing the upper critical end point to higher P (Boettcher 1984).

Lower-crustal and upper-mantle fluids may also contain high concentrations of salts, particularly NaCl (Touret 1985; Keppler 1996; Newton et al. 1998; Newton and Manning 2010; Manning and Aranovich 2014). Unlike CO_2, quartz solubility at constant T initially increases with the addition of NaCl at low P (Novgorodov 1977; Xie and Walther 1993; Evans 2007). In contrast, isothermal addition of NaCl to H_2O at $P > 5$ kbar causes quartz solubility to decline (Newton and Manning 2000; Shmulovich et al. 2001), as in CO_2. Similar effects are seen with other salts (Shmulovich and Graham 2004; Shmulovich et al. 2006). Aranovich et al. (2013) showed that addition of NaCl increases the melting T of simple granite; however, the effects of salt addition on quartz melting and near-solidus solubility have not previously been investigated in the system SiO_2–H_2O–NaCl.

We carried out experiments on quartz solubility and melting in the system SiO_2–H_2O–NaCl at 15–20 kbar, 900–1100 °C. The results constrain the solubility changes as a function of NaCl concentration, the hydration state of solute silica species, and the trajectory of the ternary critical curve. The work gives insights into the chemical controls on critical mixing of silicate liquids and crustal fluids.

Experimental methods

Experimental methods generally followed Manning and Boettcher (1994) and Newton and Manning (2000). Two types of experiment were conducted, weight-loss experiments and phase-field mapping experiments. Weight-loss experiments involved determination of equilibrium SiO_2 concentration by the mass lost from a single quartz crystal. Where solubility was extremely high or evidence for two fluids was detected, the locations of phase boundaries were constrained by limiting runs showing the presence or absence of a phase of interest.

Starting materials

Starting materials included natural, high-purity quartz (Manning 1994), reagent-grade NaCl (baked at 310 °C for ≥20 min to boil off any H_2O that might affect accurate weighing), and millipure H_2O. For single-crystal solubility experiments, an inclusion-free, optically transparent quartz crystal was chipped into a small, rough, equant block and then ground with a diamond file into an ellipsoid. Using 100-, 320-, 600-, and 2400-grit aluminum oxide emery paper successively, the grain was brought to a fine polish (Fig. 1a). Quartz ellipsoids of 1–4 mg mass were found to be optimal; larger grains tended to fracture. More than one crystal was used in experiment 18 because for the amount of quartz needed to saturate the fluid, we expected several small crystals to fare better than a single large crystal. In other runs, quartz powder was added with the single quartz crystal in an amount less than the expected dissolved SiO_2 concentration. The powder was made by grinding high-purity natural crystals and separating the finest particles (~290 mesh) by elutriation. The high-surface-energy powder dissolves quickly relative to the single crystal, producing an effective initial fluid that is closer to quartz saturation and dissolves less of the large quartz crystal. This increased the probability that the crystal was preserved.

Capsule loading

Each capsule was made from 1.8-cm-long segments of 3.5 mm diameter, 0.18 mm wall thickness Pt tube. Prior to loading of starting materials, the tube was crimped at one end and sealed by arc welding with a carbon electrode. Quartz and NaCl were each added and weighed. H_2O was then introduced by syringe. Usually, a slight excess of H_2O was added, and the capsule was weighed repeatedly as the water evaporated to within ~10 μg of the target weight for the desired X_{NaCl}. The open end of the capsule was then carefully crimped to arrest further water evaporation and then sealed by arc welding. Pre- and post-weld weighings showed minimal weight loss, usually less than 0.5 mg. The weight loss of the top-weld was of similar magnitude to that of the bottom-weld on the dry, empty Pt tube segment, indicating that the weight loss during the top-weld is chiefly due to platinum evaporation. This was confirmed by checking H_2O mass balance after experiments (see below).
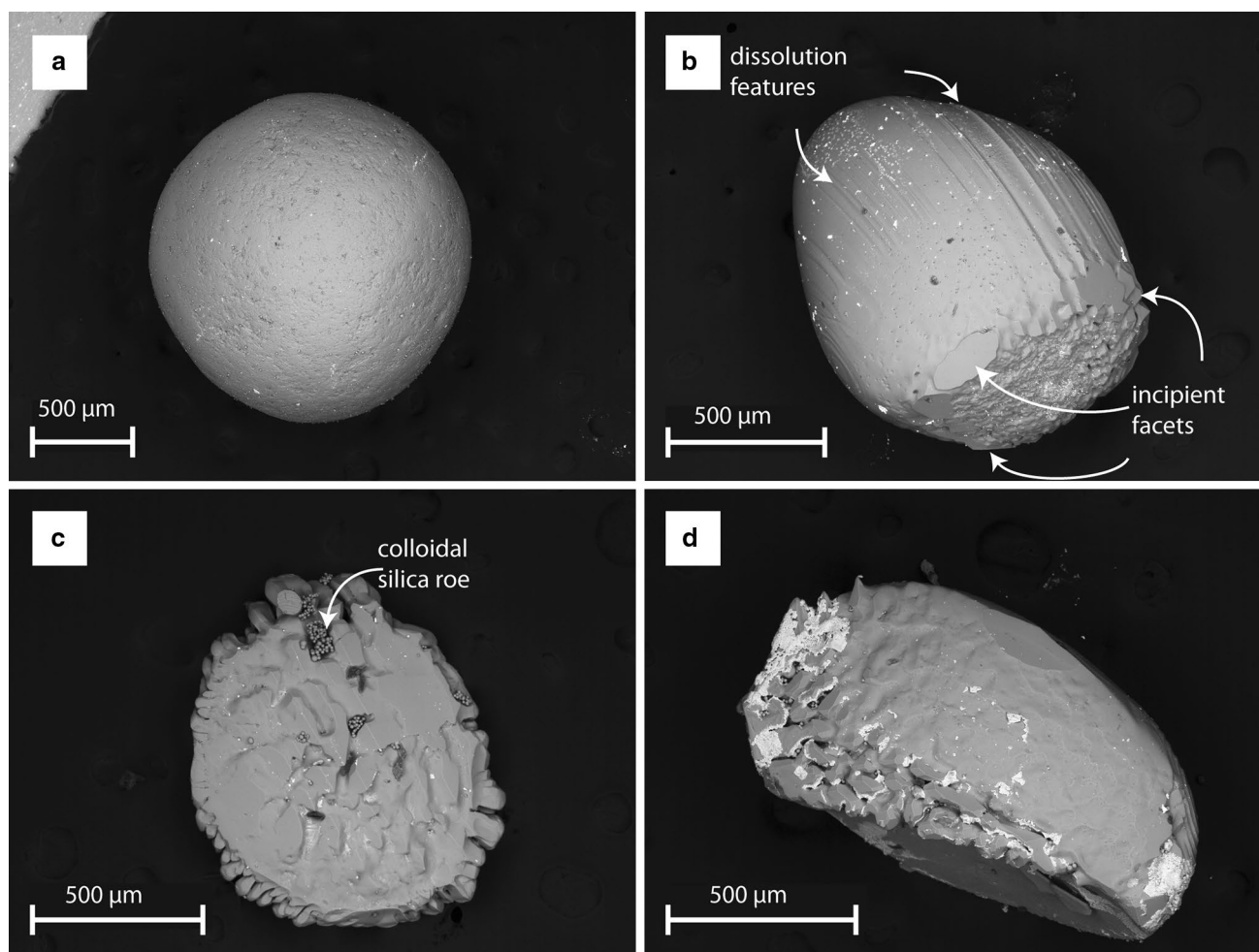
Fig. 1 Backscattered electron photomicrographs of quartz crystals. **a** Quartz grain prior to run, lacking dissolution and reprecipitation features of any kind. **b** Typical post-run quartz grain from experiment 07 shows evidence of dissolution as well as incipient crystal faces. *Small bright spots* are residual NaCl present in insufficient quantities to affect final weight. **c** Run product grain from which more than 90 % of the original mass was dissolved (experiment 44). The disk-like shape, wormy surface texture, and coliform protrusions are found only in strongly dissolved crystals. Colloidal quench roe occupies some of the crevices. **d** Large fragment of a quartz grain that broke during experiment 06. *Bright areas* are residual NaCl. Breakage and incomplete NaCl removal result in a minimum solubility constraint (Table 1)

Experimental apparatus and pressure–temperature control

Capsules were packed in 1-in. diameter NaCl–graphite furnaces (Manning and Boettcher 1994) and loaded into a piston–cylinder press. Experiments used cold piston-out conditions, wherein pressure was applied first by pumping, then by heating the sample to the target temperature, which in turn causes thermal expansion of the pressure medium to reach the target pressure. During runs, some bleeding was required to maintain thermal equilibrium of the press and hydraulic oil. Pressure was measured on bourdon-tube Heise gauges with a ± 0.3 kbar uncertainty. Temperature was controlled to ± 1 °C with Pt–$Pt_{10}Rh_{90}$ thermocouples. Reported temperatures do not take into account uncertainty resulting from pressure effects on EMF as these are not well quantified, but they likely introduce temperature errors no greater than 2.5–10 °C (Getting and Kennedy 1970; Cheng et al. 1975).

Post-experiment analysis

Runs were quenched rapidly by cutting power to the apparatus. Temperature dropped to 200 °C within 20 s. The extracted capsule was weighed and compared with its pre-run weight; discrepancies less than 100 µg were taken as sufficient evidence that no significant leakage of capsule contents occurred. Furthermore, post-run H_2O content was determined for most experiments by measuring weight loss of the capsule after puncturing with a needle and drying on

a watch glass for 15 min at 115 °C, then 15 min at 310 °C. Where determined, H_2O-out differs from H_2O-in by less than 3 % (Table 1), supporting the assumption that negligible H_2O was lost during welding or experiments.

In weight-loss experiments, dried capsules were opened and their contents emptied into a watch glass. Contents were rinsed to remove halite from quartz and quench colloidal silica (referred to as "roe"; Kennedy et al. 1962). The quartz was separated from the quench roe and weighed, either as a single intact crystal or, if broken, as the collected fragments.

At 1100 °C where two fluid phases were present, solubility determinations by weight loss were with one exception (run 52) not feasible because separation of quartz from quenched glass was unreliable. Phase boundaries were in these cases constrained using textural analysis to determine the phases present at run conditions. After quenching, opened charges were inspected for the presence or absence of quartz, glass, and quenched colloidal silica. Water mass balance could not be checked directly, but since H_2O loss was negligible in weight-loss experiments, the phase-field mapping runs were considered to have held water unless the post-run capsule weight was substantially less than the pre-run weight.

In selected experiments at 1100 °C, the pH of the quench fluid was measured to detect excess Cl^- relative to Na^+ in the residual fluid (see below). A pH strip was held with the reactive side against the capsule; the capsule was punctured through the back of the strip. Quench fluids were rapidly expelled to contact the pH indicator surface.

Quenched glass from selected experiments was analyzed by electron microprobe. Analytical conditions for wavelength dispersive analysis included a focused beam, a beam current of 15 nA, an accelerating voltage of 15.0 kV, and a measuring time of 20 s for Si, Al, and Cl. For Na, measuring time was shortened to 10 s. Standards were quartz (Si), anorthite (Al), Tiburon albite (Na), and synthetic barium chlorapatite (Cl).

Uncertainty

Sources of uncertainty include weighing errors, which were quantifiable, and other experimental and observational factors that could not be quantified. Weights were measured either on a Mettler M3 microbalance ($1\sigma = 2$ µg) or on a Mettler UMX2 ultramicrobalance ($1\sigma = 0.2$ µg). Uncertainties resulting from weighing errors were propagated to calculate molality (m_{SiO_2}), mole fraction (X_{NaCl}, X_{H_2O}, X_{SiO_2}), activity (a_{H_2O}, a_{SiO_2}), and log of activity.

Undetected quartz grains are a potentially important source of inaccuracy. There are two ways such crystals might be produced. Previous hydrothermal piston–cylinder experimental studies showed that minute, new crystals occasionally nucleate during runs (Caciagli and Manning 2003; Tropper and Manning 2005; Antignano and Manning 2008a, b). Termed "vapor-transport crystals," these grains nucleate after long run times because of small temperature gradients. Small crystals that are challenging to detect and retrieve may also be produced when the starting crystal breaks during an experiment. Either way, such crystals lead to erroneous solubility determination using weight-loss methods. Problems with detection of vapor transport or fragmented crystals were minimized by keeping run times as short as possible consistent with establishing equilibrium, and by thorough inspection of capsule contents under high magnification when crystals returned broken. However, to be reliably detected, retrieved and weighed, crystals had to be sufficiently large and texturally distinct to be distinguishable from 10- to 20-µm-diameter quench-roe spherules. In practice, grains more than twice this radius could be readily distinguished from quench roe. The magnitude of any uncertainty resulting from detection failure can be assessed as an example using experiment 09, which gave the lowest solubility in this study (0.648 molal). Failure to detect a 20-µm-radius quartz sphere in an experiment with 13.549 mg H_2O, translates to a solubility error of 1.1×10^{-4} molal. Approximately 60 such grains would need to go undetected to generate a 1 % error in solubility. All estimated values used here are extremely conservative: increasing H_2O mass or total solubility, or decreasing the radius of undetected quartz would all only increase the number of grains that must be missed to shift reported concentrations >1 %. We conclude that even in the unlikely event that a few grains went undetected in selected runs, their masses were insufficient to materially affect reported solubilities.

Results

Results of weight-loss solubility experiments are given in Table 1. Table 2 gives results of phase-field mapping experiments.

Textures of run products

Capsules oozed salty quench fluid when punctured. The fluid ranged from translucent and colorless where solute concentration was low, to milky white where solute concentration was high. After drying and opening, the residue from the evaporated quench fluid consisted of ~1 µm halite cubes and colloidal silica roe (<10 µm radius; Fig. 1c). The textures of quartz crystals were variable. When retrieved intact, product quartz crystals typically exhibited dissolution features such as striations, grooves, and other surface irregularities, and growth features such as facets (Fig. 1b).

Table 1 Results of experiments yielding quartz solubility by weight loss

Run no.	P (kbar)	T (°C)	Time (min)	H_2O in (mg)	H_2O out (mg)	ΔH_2O (%)	NaCl (mg)	X_{NaCl}	Quartz in (mg)	Quartz out (mg)	m_{SiO_2} (molal)	X_{SiO_2}	Notes
39	15	900	60	17.294	17.556	1.51	6.243	0.100	3.8641	2.2284	1.574	0.025	Short run
40	15	900	180	17.932	17.911	−0.12	6.470	0.100	3.7807	1.5767	2.046	0.032	Max
41	15	900	360	27.569			9.949	0.100	3.8378	0.9584	1.738	0.027	Min
42	15	900	360	24.901			8.999	0.100	3.6653	0.4943	2.119	0.033	
43	15	900	360	15.838	15.950	0.71	51.299	0.500	2.1539	1.1392	1.066	0.010	
01	15	950	81	24.781	24.808	0.11	35.006	0.303	6.556	4.658	1.275(2)	0.016	Min
18	15	1000	90	20.662	20.525	−0.66	3.538	0.050	12.906	5.212	6.198(3)	0.096	xl broke
04	15	1000	85	27.535			8.681	0.089	5.895	Trace	3.563(1)	0.055	Min
05	15	1000	100	24.434	24.252	−0.74	8.689	0.099	9.753	4.230	3.762(2)	0.058	
03	15	1000	105	23.568	24.041	2.01	19.908	0.207	8.563	5.675	2.039(2)	0.028	
13	15	1000	20	22.401	22.512	0.50	31.219	0.301	3.5036	1.6275	1.394	0.017	Short run
14	15	1000	40	23.161	23.299	0.60	32.265	0.300	3.6531	1.8601	1.288	0.016	Short run
02	15	1000	90	24.443	25.153	2.90	34.558	0.304	4.527	2.178	1.599(2)	0.020	
17	15	1000	90	21.444	21.686	1.13	29.887	0.301	3.9393	1.8847	1.595	0.020	
15	15	1000	180	20.977	21.110	0.63	29.238	0.301	3.3403	1.4585	1.493	0.018	
07	15	1000	90	15.631	15.750	0.76	31.907	0.386	2.7114	1.6036	1.180	0.013	
08	15	1000	90	15.489	15.611	0.79	50.904	0.503	2.0067	1.0839	0.992	0.009	
09	15	1000	105	13.549	13.693	1.06	65.042	0.597	1.8921	1.3642	0.648	0.005	
06	15	1050	60	24.813	24.903	0.36	34.014	0.297	4.459	1.312	2.111(2)	0.026	Min
11	15	1050	110	14.966	15.413	2.99	31.758	0.395	3.576	2.2885	1.432(2)	0.015	
12	15	1050	120	18.017	18.166	0.83	59.078	0.503	3.1560	1.9412	1.122	0.010	
48	15	1080	90	13.454	13.500	0.34	18.716	0.300	3.3471	1.5373	2.239	0.027	
49	15	1090	90	13.447	13.474	0.20	18.745	0.301	2.8778	0.9046	2.442	0.030	
52	15	1100	97	2.245			7.182	0.497	7.4225	6.8158	4.498	0.039	pH = 7; xl broke
44	20	1000	120	19.839			7.187	0.100	6.1855	0.5288	4.746(1)	0.071	
46	20	1000	180	24.523	24.307	−0.88	34.117	0.300	5.4482	Trace	3.698(1)	0.045	Max
45	20	1000	180	15.136			49.149	0.500	1.3211	0.5103	0.892	0.008	

H_2O in and H_2O out correspond to weights at beginning and end of experiment, respectively. Calculated values use H_2O in. Weights given to four decimal places were measured on a Mettler UMX2 ($1\sigma = 0.2$ μg); those given to three decimal places were measured on a Mettler M3 ($1\sigma = 2$ μg). Parenthetical values represent propagated 1σ weighing error in final digit of SiO_2 molality and activity (omitted if $<5 \times 10^{-4}$). Errors in X_{NaCl} are $<5 \times 10^{-5}$. Max, run yielded maximum solubility only; Min, run yielded minimum solubility only; pH, quench pH (see text); xl broke, solubility determined by collecting and weighing broken crystal; Short run, short-duration experiment used only to establish time to equilibration (Fig. 2)

Table 2 Results of phase-field mapping experiments

Run no.	P (kbar)	T (°C)	Time (min)	H_2O in (mg)	NaCl (mg)	X_{NaCl} in	Qtz in (mg)	Products	Quench pH	Interpretation
53	12.5	1100	85	11.853	2.023	0.050	36.494	$q + g + r$	1	$q + 2$ fluids
50	15	1100	62	2.856	1.035	0.100	9.553	$q + g + r$		$q + 2$ fluids
54	15	1100	60	14.914	2.451	0.048	48.805	$q + g + r$	1	$q + 2$ fluids
51	15	1100	80	5.862	0.999	0.050	19.282	$q + g + r$		$q + 2$ fluids
47	15	1100	75	13.772	19.071	0.299	3.440	$q + g + r$		$q + 2$ fluids
2.1	15	1100	80	7.479	3.293	0.120	4.970	$g + r$		2 fluids
2.2	15	1100	80	3.619	8.193	0.411	7.044	$q + r$		$q + 1$ fluid
2.3	15	1100	80	3.355	2.988	0.215	3.092	$q + g+r$		$q + 2$ fluids
2.4	15	1100	80	4.532	6.295	0.300	1.171	$q + g+r$	1	$q + 2$ fluids

Abbreviations in product phases column are for quartz (q), glass (g), and colloidal silica roe (r). High P–T phases inferred from run products are listed in the interpretation column as "$q + 1$ fluid" where run products contained quartz and roe, but no glass, "$q + 2$ fluids" where run products contained quartz with both roe and glass, and "2 fluids" where quartz was absent but roe and glass were present

Unusual textures developed where solubility was very high, for example, in experiment 44, in which ~90 % of the original crystal dissolved, the post-run residual crystal was pancake-shaped, with irregular topography (Fig. 1c). When quartz crystals broke, the fragments typically consisted of a few large pieces (Fig. 1d) and several small, euhedral crystals.

Equilibrium

It is assumed that equilibrium held where solubility was independent of time (Manning 1994; Newton and Manning 2000). The time required to attain a constant, time-independent solubility was assessed in two sets of experiments at 15 kbar, at 900 and 1000 °C (Fig. 2). Constant solubility was achieved by 180 min in duration at 900 °C, and by 90 min at 1000 °C. Run times were at least this long, with three exceptions (Table 1). Experiment 04 ran for 85 min at 1000 °C. Only unweighable traces of the original quartz crystal remained. If equilibrated, the total weight of the starting quartz crystal would give a maximum solubility; however, it is possible that a longer run duration would have led to complete dissolution so this experiment is treated as a constraint on minimum solubility. Solubilities derived from experiments 01 (81 min, 950 °C) and 06 (60 min, 1050 °C) are treated as minimum values due to their short durations. Phase-field mapping experiments at 1100 °C were not reversed; however, run durations were assumed adequate for generation of the stable phase assemblage.

Quartz solubility

Results of experiments in which quartz solubility was determined by weight loss are shown in Fig. 3. In pure
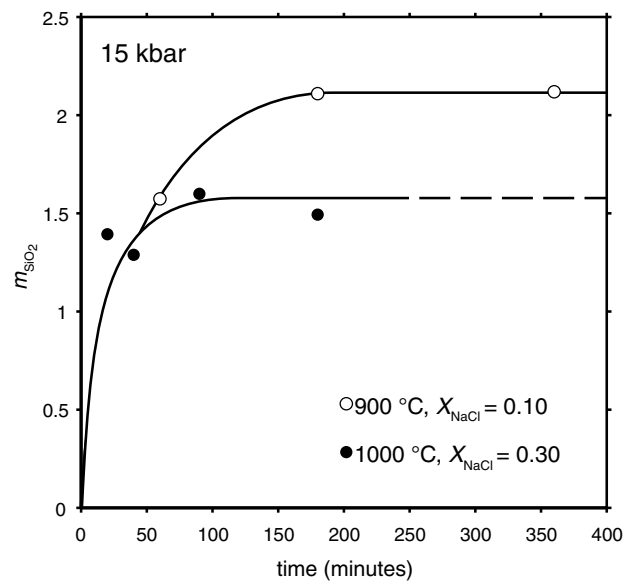
Fig. 2 Variation in quartz solubility with time at 15 kbar, at 900 °C, $X_{NaCl} = 0.1$, and 1000 °C, $X_{NaCl} = 0.3$. The results demonstrate achievement of a steady state after 180 min at 900 °C and 90 min at 1000 °C. Propagated weighing uncertainties are smaller than symbol size (Table 1)

H_2O at 15 kbar, silica solubility increases from 0.061 X_{SiO_2} at 900 °C to 0.301 at 1050 °C (Hunt and Manning 2012). At 1000 °C, X_{SiO_2} rises from 0.174 at 15 kbar to 0.295 at 20 kbar. Results of the present study show that at fixed P and T, X_{SiO_2} initially decreases strongly with increasing X_{NaCl} but then declines more gradually at high X_{NaCl} (Fig. 3). At high X_{NaCl}, the declines are approximately exponential, but the initial solubility drops are steeper. At fixed X_{NaCl}, quartz solubility increases with P and T, as in pure H_2O.

Fig. 3 Quartz solubility as a function of NaCl mole fraction. **a** Silica mole fraction at 15 kbar, 900–1050 °C. **b** Results at and 15 and 20 kbar, 1000 °C. *Circles* equilibrium solubility determination; *up- and down-pointing triangles* minimum and maximum solubility constraints. Short-duration runs (Table 1) are not plotted. *Trend lines* were drawn by eye. Data at $X_{NaCl} = 0$ from Hunt and Manning (2012). Errors in data from the present study (Table 1) are smaller than the *symbols*. At all *P* and *T*, silica mole fraction drops precipitously with initial increases in X_{NaCl}, then falls more gradually at higher X_{NaCl}
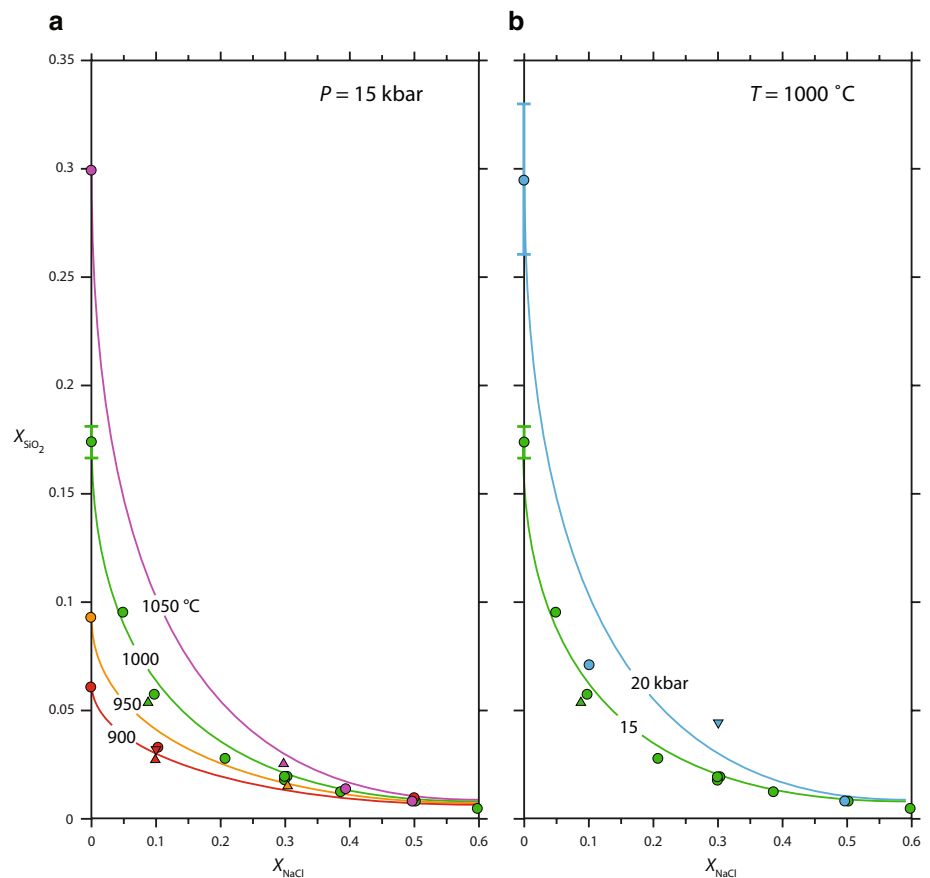
Phase-field mapping experiments

At 1100 °C (Table 2), solubilities were high and textures of quench products in some experiments revealed evidence for the presence of two fluids. Quartz solubility could not be determined by weight loss. Instead, the topology of the ternary phase diagram was determined for a range of bulk compositions by identifying phases present from quench products. In these experiments, X_{NaCl} refers to that of the bulk composition in the charge, because where two fluids were present, X_{NaCl} could not be determined for each fluid individually. All experiments were conducted at 15 kbar except run 53 at 12.5 kbar.

A key feature of the experiments at 1100 °C is the result that the more silica rich of the two coexisting fluids quenches to glass, even where inferred H_2O contents of the fluid may be quite high. Quench glass was observed in all experiments at $X_{NaCl} \leq 0.3$. The vesiculated, milky glass was found in intergranular regions where quartz recrystallized to polycrystalline aggregates (Fig. 4a) and in a few clumps of spheroids ranging from 10 to 60 µm in diameter (Fig. 4b) in the portion of the charge occupied by the fluid. In addition, experiments at all X_{NaCl} contained quench silica roe that was ≤10 µm in diameter and evenly distributed

throughout the charge. The presence of large intergranular and spheroidal glass masses is interpreted to indicate the presence of two fluids—one hydrous and Si rich, the other saline and relatively Si poor—at experimental run conditions.

The quench pH was measured in four runs near the interpreted boundary of the two-fluid field. Three experiments containing evidence for the coexistence of two fluids had quench pH 1 (Table 2). In contrast, run 52 at 1090 °C and $X_{NaCl} = 0.3$ contained no glass and yielded a quench pH of 7 (Table 1). Thus, there is a correlation between acidic quench fluid and the presence of large glass masses that coexist with smaller quench roe.

Electron microprobe analyses of selected quenched glasses are given in Table 3. Glasses were analyzed at spots selected to avoid vesicles visible on the polished surface of the glass (Fig. 4). Oxide totals from vesicle-free zones ~89–95 wt%. Water contents implied by these oxide totals are significantly lower than suggested by the phase relations (see below), indicating that regardless of small variations, all glasses lost substantial H_2O on quench. All glass analyses with oxide totals >89 wt% showed Na/Cl >1. Preferential partitioning of Na over Cl yields excess Cl in the coexisting fluid, which when quenched would have low
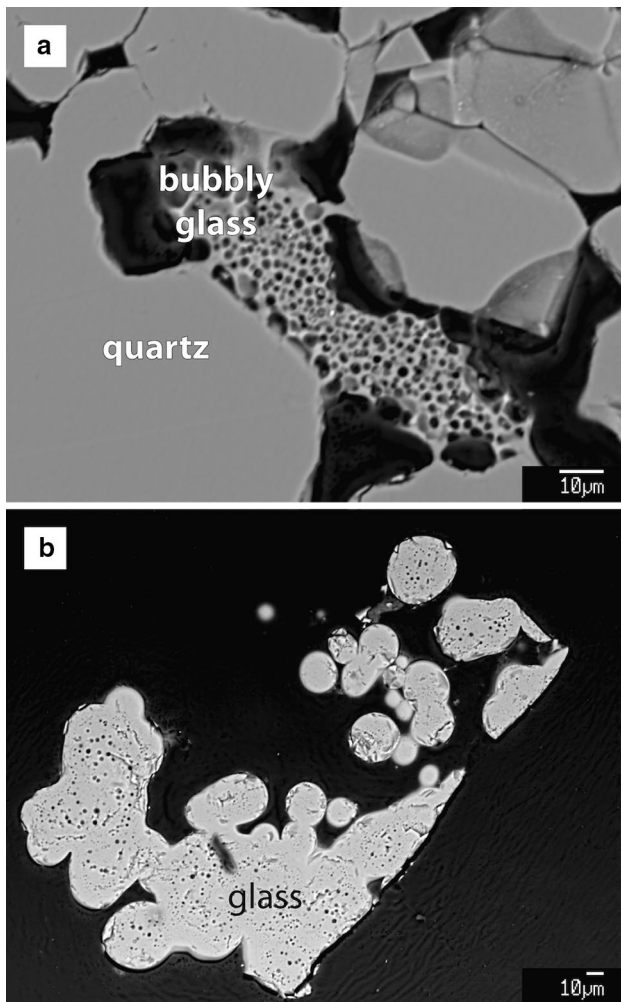
Fig. 4 Backscattered electron photomicrographs showing textures of glasses quenched from silica-rich fluid in experiments in which two fluids are inferred to coexist. **a** Vesiculated quench glass in pore space between quartz grains in Run 54 ($X_{NaCl} = 0.048$, 1100 °C, 15 kbar). **b** Vesiculated spheroidal glass aggregates retrieved from crystal-free portion of the capsule in Run 50 ($X_{NaCl} = 0.1$, 1100 °C, 15 kbar)

pH. This explains the shift from neutral pH to acidic pH of quench fluids when a second fluid phase appears, and supports the use of quench pH as a guide to the phase relations.

Several glass analyses gave significantly lower totals of <83 wt% and had Na < Cl. This is interpreted to be an artifact of inaccuracies due to Na volatilization and/or inclusion of subsurface vesicles in the analyses. These analyses are not reported in Table 3. Electron microprobe analyses also revealed minor Al_2O_3 in the silica-rich glasses. The source was most likely a combination of trace impurity of the natural quartz and the aluminum oxide emery paper with which the pre-run quartz crystals were ground and polished. No differences were observed that depend on variations in Al_2O_3 content, so we infer that presence of minor Al_2O_3 does not affect phase relations or solubility.

Interpretive phase relations at 1100 °C and 15 kbar are shown in Fig. 5. With the exception of experiment 2.1, runs with bulk X_{NaCl} of 0.05–0.30 contained three quench materials: quartz, silica-rich glass, and quench silica roe. These runs were used to define the limits of a three-phase field in which quartz is stable with a siliceous fluid and a saline fluid (Fig. 5). Run 2.1 had bulk $X_{NaCl} = 0.102$ but a higher bulk H_2O/SiO_2, and it returned silica-rich glass and colloidal silica roe but no quartz. This composition is therefore interpreted to lie in the two-fluid field. Two experiments at bulk $X_{NaCl} > 0.3$ contained quartz and quench roe, but silica-rich glass was not detected. These bulk compositions are interpreted to lie in the stability field of quartz + saline fluid. Run 52 (Table 1) yielded a quantitative constraint on quartz solubility. In this case, the measured fluid composition is plotted (rather than its bulk composition); this determines the location of the solubility curve at high X_{NaCl}. All other phase boundaries are approximate while remaining consistent with constraining bulk compositions.

Runs at $X_{NaCl} = 0.3$ and 15 kbar revealed no quenched glass at 1090 °C, whereas quenched glass was seen at

Table 3 Electron microprobe analyses of quenched glasses

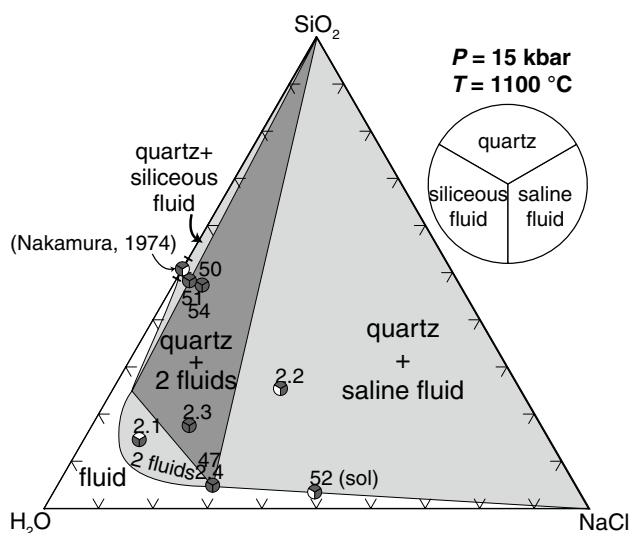| Run	54	54	54	53	50	50	50
Spot	2	3	9	10	16	17	18
SiO_2	85.78	86.52	85.24	95.34	90.36	87.32	88.86
Al_2O_3	5.14	4.12	5.31	0.13	1.00	1.12	1.07
Na_2O	0.94	0.77	0.90	0.07	0.34	0.32	0.27
Cl	0.03	0.05	0.04	0.04	0.20	0.33	0.25
O=Cl	0.01	0.01	0.01	0.01	0.05	0.07	0.06
Total	91.89	91.44	91.47	95.58	91.85	89.02	90.40
Na/Cl	35.88	19.50	26.94	1.96	2.00	1.13	1.25

Oxide concentration in wt%; Na/Cl is molar

Fig. 5 SiO_2–H_2O–NaCl ternary diagram showing experimental results and inferred phase fields at 15 kbar and 1100 °C. Each circle is divided into three sectors which are filled to reflect observed phase assemblage and, with two exceptions, are plotted (molar units) at the bulk composition of the experiment. The exceptions are run 52 and the datum from Nakamura (1974), in which quartz solubility could be determined; in these cases, the inferred fluid composition is plotted. Propagated weighing uncertainties for results of this study are smaller than symbol size. Unfilled region of ternary corresponds to the stability field for a single fluid of varying SiO_2 and NaCl content. The solubility of quartz in H_2O (Nakamura 1974) defines the NaCl-absent apex of a triangular stability field for quartz + low-NaCl siliceous fluid. At X_{NaCl} = 0.05–0.3, capsules contained quartz, silica-rich glass, and quench roe, indicating the stable coexistence of quartz with two immiscible fluids. A single experiment at high H_2O/SiO_2 (Run 2.1) contained no quartz, implying that this bulk composition was in the two-fluid stability field. Experiments at X_{NaCl} > 0.3 indicate that quartz is stable with a single, saline fluid

1100 °C. This constrains the appearance of a second fluid phase to 1095 ± 5 °C at this composition. It is likely that the two-fluid field initially appears at T < 1100 °C at bulk X_{NaCl} lower than 0.3. Run 53 at 12.5 kbar, 1100 °C, reveals the presence of quartz + two fluids at X_{NaCl} = 0.05, indicating that fluid unmixing extends to P lower than 15 kbar.

Discussion

Comparison to previous solubility results

Newton and Manning (2000) and Shmulovich et al. (2001, 2006) investigated quartz solubility in H_2O–NaCl solutions at P–T conditions relevant to the lower crust, but lower than in our study. Hunt and Manning (2012) determined quartz solubility in H_2O at P and T similar to those of the present work, but variations in solvent composition were not explored. Newton and Manning (2000) found that at
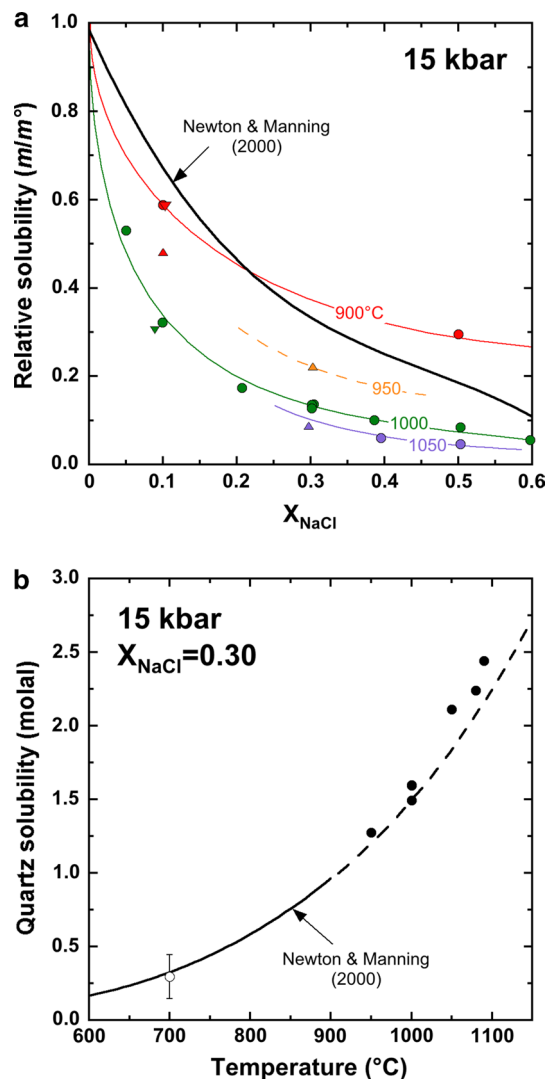

Fig. 6 a Relative solubility of quartz versus NaCl mole fraction at 15 kbar. Relative solubility corresponds to ratio of molality at a given T and X_{NaCl} (m) divided by molality in pure H_2O at the same T ($m°$, see text). *Symbols* for data from the present study as in Fig. 3. Propagated weighing uncertainties are smaller than symbol size. *Black line* is predicted dependence on X_{NaCl} at all T (Newton and Manning 2000). The disagreement between results of the present study and the prediction of Newton and Manning (2000) implies that excess silica is present in solution (see text). **b** Quartz solubility versus temperature at 15 kbar and X_{NaCl} ~ 0.3. *Filled circles* data from the present study; *open circle* from Newton and Manning (2000) (1σ error). Data from the present work lie at slightly higher solubility than predicted by the extrapolation of the equation of Newton and Manning (2000) (*solid curve*)

P greater than about 5 kbar, solubility of quartz decreases exponentially with rising X_{NaCl}. We observed qualitatively similar decreases with increasing NaCl concentration at the higher P and T of our study (Fig. 3). However, Newton and Manning (2000) showed that the relative solubility—defined as the molality of SiO_2 (m) at a given X_{NaCl} and T relative to that in pure H_2O ($m°$)—displayed a

temperature-independent decline with increasing X_{NaCl} at 2–10 kbar and 500–900 °C. Their equation describing this dependence can be extrapolated to 15 kbar and $T > 900$ °C. Figure 6a compares the resulting prediction to relative solubilities from the present study at 15 kbar and 900–1050 °C. It can be seen that our data do not lie on the Newton and Manning (2000) curve. Moreover, our data imply a systematic decrease in $m/m°$ with T at a given X_{NaCl}. The Newton and Manning (2000) model was developed for P and T where subsequent studies showed that silica species in solution were limited to monomers and dimers (Newton and Manning 2002, 2003). In contrast, at the high P and T of the present work, more polymerized species are also present and quartz solubility is correspondingly higher (Newton and Manning 2008; Hunt and Manning 2012). The systematic, generally negative departure of our data from the Newton and Manning (2000) curve is consistent with higher-than-predicted quartz solubility in pure H_2O ($m°$).

This hypothesis can be assessed at 15 kbar and $X_{NaCl} = 0.3$. Figure 6b illustrates that quartz solubilities from the present study show a similar increase with T, and are only slightly higher than predicted by the extrapolation of the Newton and Manning (2000) model. Thus, the large discrepancies indicated in Fig. 6a must arise from substantially greater $m°$ than is accounted for in the Newton and Manning (2000) model.

Silica solubility and speciation in H_2O–NaCl fluids

At high P and T, aqueous silica at near-neutral pH may exist in a wide range of species, including monomers ($Si(OH)_4$), dimers ($Si_2O(OH)_6$), and higher-order oligomers (Zhang and Frantz 2000; Zotov and Keppler 2000; Newton and Manning 2002, 2003; Gerya et al. 2005, 2008; Mysen 2010; Mysen et al. 2013; Hunt and Manning 2012). The relative abundance of these species varies with P, T, total dissolved silica, and H_2O activity. Walther and Orville (1983) and Newton and Manning (2009) showed that the variation in quartz solubility with X_{H_2O} in H_2O–NaCl and H_2O–CO_2 fluids gave insights into the speciation of aqueous silica and its hydration by H_2O molecules. Newton and Manning (2009) found that, in H_2O–CO_2 fluids over a wide range of metamorphic P and T, aqueous silica species are dominated by the monomer and the dimer, and that these species were solvated by 2.0 H_2O per Si. When the additional two H_2O per Si needed to form hydroxyl groups are included, the monomer possesses an average hydration number of 4.0. In contrast, in H_2O–NaCl fluids at 800 °C, 10 kbar, Newton and Manning (2006) inferred that the average hydration number of the $Si(OH)_4$ monomer is 1.9, suggesting that dissolved NaCl significantly reduces the average hydration number of H_2O relative to CO_2. However, while the effects of CO_2 on H_2O hydration appear to

be independent of P and T (Newton and Manning 2009), it is unclear whether the same is true for NaCl. Moreover, the consequences of higher-order silica oligomers at P and T near hydrous melting (Newton and Manning 2008; Hunt and Manning 2012) have not been examined. Addressing these issues requires numerous determinations of solubility over a wide range of X_{NaCl}. The data at 1000 °C and 15 kbar in the present study can be used for such an analysis.

Following Walther and Orville (1983) and Newton and Manning (2006, 2009), the average hydration number n of the silica monomer, $Si(OH)_4$, can be derived by simplifying its stoichiometric representation to $SiO_2{\cdot}nH_2O$ and considering its equilibrium with quartz

$$\underset{\text{quartz}}{SiO_2} + nH_2O = \underset{\text{monomer}}{SiO_2 \cdot nH_2O} \tag{1}$$
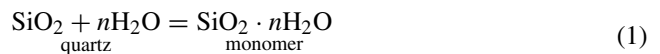
The equilibrium constant K_{qm} for Eq. 1 is

$$K_{qm} = \frac{a_m}{a_{H_2O}^n} \tag{2}$$

where a_m and a_{H_2O} are, respectively, the activities of the silica monomer and H_2O, the standard state of quartz is unit activity of the stoichiometric phase at any P and T, and quartz is assumed to be pure. This leads to

$$\log a_m = n \log a_{H_2O} + \log K_{qm} \tag{3}$$

If silica monomers were the only form of dissolved SiO_2, n could be derived from the variation in the solubility of quartz with fluid composition (Walther and Orville 1983). However, the high-PT polymerization of aqueous silica to dimers and higher-order oligomers requires an activity model for dissolved silica. Newton and Manning (2009) determined the activity of the total dissolved silica from quartz solubility measurements at conditions where aqueous silica species other than monomers and dimers were negligible. Under such conditions, the distribution of silica species is governed by the equilibrium

$$\underset{\text{monomer}}{2SiO_2 \cdot nH_2O} = \underset{\text{dimer}}{Si_2O_4 \cdot (2n-1)H_2O} + H_2O \tag{4}$$
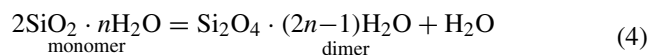
Taking the standard states of the monomer and dimer (d) to be unit mole fraction of the respective species, and assuming ideal mixing of aqueous species (Newton and Manning 2002, 2003, 2006, 2008, 2009), the equilibrium constant for Eq. 4 is

$$K_{md} = \frac{X_d a_{H_2O}}{X_m^2} \tag{5}$$

Newton and Manning (2009) derived an empirical expression for Eq. 5, which can be extrapolated to 1000 °C, 15 kbar to give $K_{md} = 638$.

Following Newton and Manning (2006, 2008, 2009), the standard state for total dissolved SiO_2 is taken to be unit

Table 4 Calculated mole fractions and activities at 1000 °C, 15 kbar assuming ideal fused salt behavior

Run	a_{H_2O}	a_{NaCl}	X_{SiO_2}	a_{SiO_2}
	1		1.740×10^{-1}	1.129×10^{-2}
18	0.905	0.182	9.173×10^{-2}	7.716×10^{-3}
4	0.837	0.299	5.101×10^{-2}	5.466×10^{-3}
5	0.820	0.327	5.266×10^{-2}	5.505×10^{-3}
3	0.658	0.568	2.359×10^{-2}	3.238×10^{-3}
2	0.534	0.715	1.516×10^{-2}	2.319×10^{-3}
17	0.538	0.711	1.522×10^{-2}	2.330×10^{-3}
15	0.538	0.711	1.426×10^{-2}	2.250×10^{-3}
7	0.443	0.804	9.321×10^{-3}	1.633×10^{-3}
8	0.330	0.891	5.868×10^{-3}	1.110×10^{-3}
9	0.253	0.936	2.942×10^{-3}	6.704×10^{-4}

a_{H_2O}, a_{NaCl}, X_{SiO_2} calculated from Eqs. 9, 10, and 11, respectively, using X_{H_2O} and X_{NaCl} from Table 1. a_{SiO_2} from Eq. 8 using $K_{md} = 638$ (see text). Value of X_{SiO_2} in pure H_2O is from Hunt and Manning (2012). Only ≥90 min runs included (see Table 1)

activity of the hypothetical solution of pure monomers, and monomers and polymerized species are assumed to mix ideally. This leads to:

$$a_{SiO_2} = \gamma_{SiO_2} X_{SiO_2} = X_m = a_m \tag{6}$$

where γ_{SiO_2} and X_{SiO_2} are the activity coefficient and mole fraction of total silica dissolved in solution. Sodium–silica species and NaCl–SiO_2 species, inferred in low-density solutions (Evans 2007, Newton and Manning 2016), are assumed negligible at the conditions of the present work. Combining Eqs. 5 and 6 and the mass balance constraint,

$$X_{SiO_2} = X_m + 2X_d \tag{7}$$

yields

$$a_{SiO_2} = \frac{\left(1 + 8X_{SiO_2} K_{md}/a_{H_2O}\right)^{1/2} - 1}{4K_{md}/a_{H_2O}} \tag{8}$$

The activity model was optimized for the limited data set available, but Newton and Manning (2008) showed that it can be used to obtain thermodynamically consistent mixing relations for the system SiO_2–H_2O.

Aranovich and Newton (1996) found that, at 600–850 °C, NaCl in H_2O–NaCl solutions progressively dissociates with increasing P, and that at 10–15 kbar the salt is fully dissociated. They derived an activity model for H_2O and NaCl using an ionization parameter, α, which nominally varies from zero in fully associated solutions to one in fully dissociated solutions. The parameter α was treated as an empirical fit parameter, but the range over which it can be extrapolated and yield valid predictions is uncertain, and it does not vary with NaCl concentration, so its utilization at 1000 °C and 15 kbar is problematic. However, Aranovich

and Newton (1996) showed that, where NaCl is fully dissociated, the solution closely approaches ideal fused salt behavior, for which

$$a_{H_2O} = \frac{X_{H_2O}}{2 - X_{H_2O}} \tag{9}$$

and

$$a_{NaCl} = \frac{4X_{NaCl}^2}{(1 + X_{NaCl})^2} \tag{10}$$

The NaCl solutions are likely to be fully dissociated at 1000 °C and 15 kbar, so Eqs. 9 and 10 can be used to determine H_2O and NaCl activities. Similarly, the mole fraction of SiO_2 in a fused salt solution differs from that calculated using only the bulk components SiO_2, H_2O, and NaCl (Table 1). Accordingly, for an ideal fused salt solution, X_{SiO_2} in Eqs. 6–8 is

$$X_{SiO_2} = \frac{m_{SiO_2}}{m_{SiO_2} + 55.51\left(1 + \frac{2X_{NaCl}}{X_{H_2O}}\right)} \tag{11}$$

(Newton and Manning 2006), where X_{NaCl} and X_{H_2O} are the bulk mole fractions in the solution neglecting minor dissolved silica.

Values of a_{SiO_2} were calculated for data at 1000 °C and 15 kbar using Eqs. 8–11 and $K_{md} = 638$ (Table 4). Figure 7a shows that $\log a_{SiO_2}$ increases linearly with $\log a_{H_2O}$ at low a_{H_2O} but that values calculated for experiments at $\log a_{H_2O} > -0.1$ depart from this trend to higher a_{SiO_2}.

The calculation of a_{SiO_2} using the above model is based on the assumption that only silica monomers and dimers are present in solution, which should be reasonable at the lowest SiO_2 concentrations (i.e., lowest a_{H_2O}). This inference is supported by Raman spectroscopic studies of aqueous silica at high P and T (Mysen et al., 2013), which shows that where SiO_2 concentration is below quartz saturation—such as at equilibrium with forsterite + enstatite—only monomers and dimers were detected at 700–900 °C, 4–38 kbar. However, Hunt and Manning (2012) found that at higher SiO_2 concentration associated with quartz saturation in H_2O at 1000 °C and 15 kbar, dissolved Si must involve higher-order silica oligomers as well. This is again consistent with Mysen et al. (2013), who found that ring trimers were also abundant at the high SiO_2 concentrations associated with quartz saturation at T of 700–900 °C, 16–54 kbar. We therefore anticipate a change from a mixture in which species other than monomers and dimers are negligible, to one in which higher oligomers become significant. Figure 7 can be used to identify this transition.

A linear least-squares fit to the $\log a_{SiO_2}$ values at $\log a_{H_2O} < -0.1$ (Fig. 7a) yields a slope of 1.612 and an intercept of −2.02 ($R^2 = 0.996$). These values correspond,
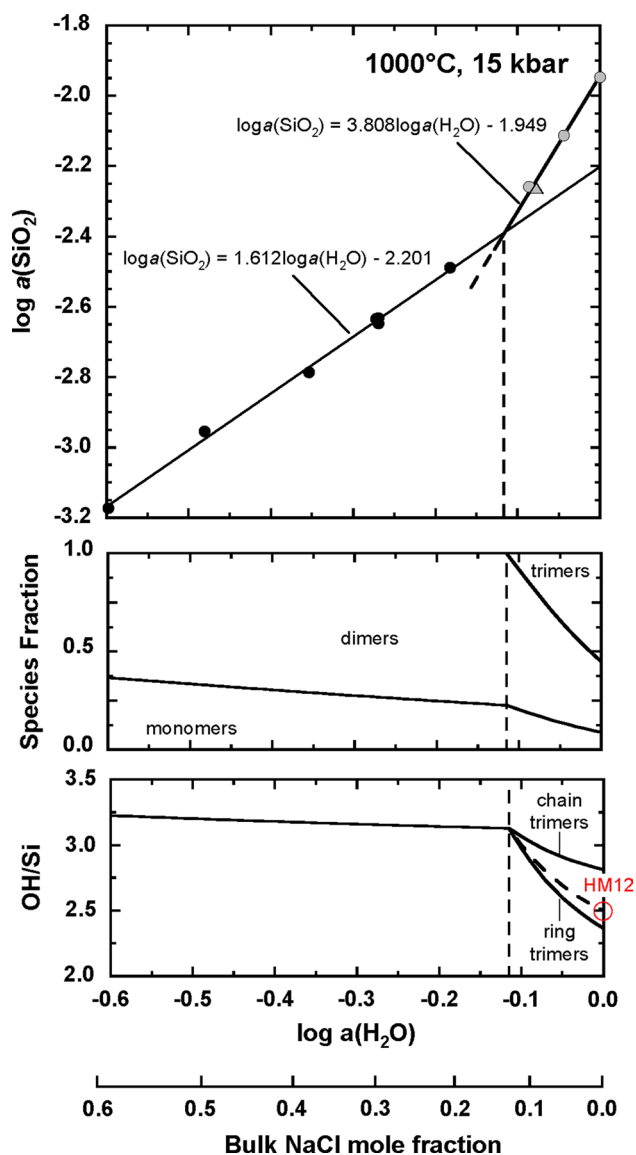
Fig. 7 **a** Variation in $\log a_{SiO_2}$ with $\log a_{H_2O}$ at 1000 °C, 15 kbar. A bulk NaCl mole fraction scale is also provided for comparison. *Black symbols* show data used to derive linear least-squares fit of $\log a_{SiO_2} = 1.612 \log a_{H_2O} - 2.202$ ($R^2 = 0.996$), which yields hydration number n and $\log K_{mq}$ (Eq. 3, see text). *Gray symbols* define a separate linear trend yielding the fit equation $\log a_{SiO_2} = 3.808 \log a_{H_2O} - 1.949$ ($R^2 = 0.989$) and an intersection at $\log a_{H_2O} = -0.115$. Value at $\log a_{H_2O} = 0$ from Hunt and Manning (2012). Propagated weighing uncertainties are smaller than symbol size. **b** Si species fractions as a function of $\log a_{H_2O}$. The linear trend at low a_{H_2O} in **a** is consistent with the presence of monomers and dimers only. The break in slope at the intersection of the two lines in **a** represents the appearance of higher-order oligomers in the solution, here assumed to be trimers (see text). **c** Variation of bulk molar OH/Si of dissolved silica species with $\log a_{H_2O}$. The ratio in monomers and dimers is 4 and 3, respectively, but differs for ring and chain trimers (2 vs. 2.67). *Solid lines* show trends assuming all trimers are either chains or rings; *dashed line* shows 70 % ring trimers, 30 % chain trimers, consistent with Hunt and Manning (2012; HM12, *open red circle*)

respectively, to n and $\log K_{qm}$ in Eq. 3. The linear increase in $\log a_{SiO_2}$ with $\log a_{H_2O}$ at low a_{H_2O} indicates that dissolved silica is successfully modeled as a mixture of monomers and dimers only, as required by Eqs. 5–8. The hydration number of 1.6 is lower than the value of 1.9 derived by Newton and Manning (2006). This further supports the inference that NaCl modifies the interaction between H_2O and SiO_2, and moreover suggests that the degree of modification changes with P and T, unlike in H_2O–CO_2 mixtures. In addition, Newton and Manning (2002) found that $\log K_{qm}$ is relatively insensitive to P and T, varying from –2.0 to –2.4 at 700–900 °C and 7–14 kbar. Our result lies within this range, though P and T were higher in the present experiments.

In Fig. 7a, the data at $\log a_{H_2O} > -0.1$ define a separate linear trend with steeper slope:

$$\log a_{SiO_2} = 3.808 \log a_{H_2O} - 1.949 \qquad (12)$$

($R^2 = 0.989$). The systematic positive departure from the linear fit to data at $\log a_{H_2O} < -0.1$ is consistent with progressively increasing abundance of additional, more polymerized species as $\log a_{H_2O}$ increases from the intersection of the two lines at $\log a_{H_2O} = -0.115$ to 0 (pure H_2O). Mass balance constraints indicate that the fraction of silica contained in the more polymerized species increases from ~0 to 67 % over this a_{H_2O} range.

The experiments do not constrain the identity of the more polymerized species, but assuming that polymerization proceeds by stabilization of progressively more networked clusters, as in silicate melts (e.g., Mysen 1988; Stebbins 1988, 1995; Mysen and Richet 2005), the most likely oligomer is a trimer. Mysen et al. (2013) identified ring trimers in their Raman spectra of quartz-saturated H_2O at similar conditions. Chain trimers are also possible, but are likely not distinguishable from dimers in Raman spectra. We will consider both. Figure 7b shows the change in the relative abundance of silica species with $\log a_{H_2O}$ assuming a mixture of monomers, dimers, and trimers. Species abundances were determined by solving Eq. 8 for X_{SiO_2} using $K_{md} = 638$ (Newton and Manning, 2009) and the fitting results in Fig. 7a, then computing the concentration of monomers, dimers, and trimers using Eqs. 5 and 6 and mass balance, and then normalizing to the total number of species. It can be seen that, at the lowest a_{H_2O}, solute silica is comprised of 63 % dimers and 37 % monomers. The fraction of dimers increases as a_{H_2O} rises, reaching 77 % at the onset of detectible trimer formation ($\log a_{H_2O} = -0.115$). As a_{H_2O} increases further, monomers and dimers decrease in relative abundance as progressively more trimers form. In pure H_2O, the mass balance constraints indicate species fractions of 9 % monomers, 36 % dimers, and 55 % trimers. It is important to

note that the sharp change in slope at the onset of trimer formation is an artifact of using two linear segments to characterize the speciation; additional experiments near $\log a_{H_2O} = -0.115$ would likely suggest a smoother variation in species abundance than is indicated by our simple model.

Hunt and Manning (2012) used the ratio of hydroxylated non-bridging oxygens (OH^-) to Si as a measure of the mean extent of polymerization in SiO_2–H_2O fluids. The OH/Si ratio decreases with increasing polymerization (formation of bridging O^{2-}), from four (100 % monomers), to three for dimers, and so on to zero for maximally polymerized anhydrous SiO_2 liquid. The evolution of OH/Si with a_{H_2O} at 1000 °C and 15 kbar in H_2O–NaCl solutions is shown in Fig. 7c. In the monomer–dimer region, the increase in dimer abundance with rising a_{H_2O} causes a monotonic decrease to OH/Si = 3.1 at the onset of trimer formation. Figure 7c shows the decrease in OH/Si assuming that trimers are either 100 % rings or 100 % chains. The OH/Si ratio of these structures differs because rings have three non-bridging oxygens, whereas chains have two. In pure NaCl-free fluid, OH/Si has decreased to 2.4 (rings) or 2.8 (chains). The model of Hunt and Manning (2012) makes no a priori assumptions about the nature of Si species and gives OH/Si = 2.5 at 1000 °C and 15 kbar, between the values predicted if trimers are either all chains or all rings. If this value can be used as a constraint on the nature of polymerized species, then it implies that 70 % of trimers are rings and 30 % chains (dashed line, Fig. 7c). It is important to note, however, that this does not take into account other species that may be present at low abundance, or uncertainties in the parameters used to calculate relative abundance of monomers and dimers. Nevertheless, it is evident that there is good agreement between the results of Hunt and Manning (2012) and those of this study.

This analysis shows that our data yield a robust constraint on the progressive polymerization of aqueous silica as a function of a_{H_2O} at a fixed P and T. Although the results are insufficient to perform similar analyses at the other conditions of this study, it is important to note that the three experiments at 1050 °C and 15 kbar also yield a linear dependence of $\log a_{SiO_2}$ on $\log a_{H_2O}$ (maximum $\log a_{H_2O} = -0.27$), but $\log a_{SiO_2}$ in pure H_2O is much higher than the intercept derived from fitting using the procedures described above. Similar observations hold for at 900 °C, 15 kbar and 1000 °C, 20 kbar, though scatter is greater. Thus, the observations made at 1000 °C and 15 kbar will likely hold true at the other P–T conditions of this investigation, though the value of a_{H_2O} at which more polymerized silica begins to appear will vary. The analysis assumes no interaction between SiO_2 and NaCl, which has been inferred at low P and high T (Evans 2007; Newton and
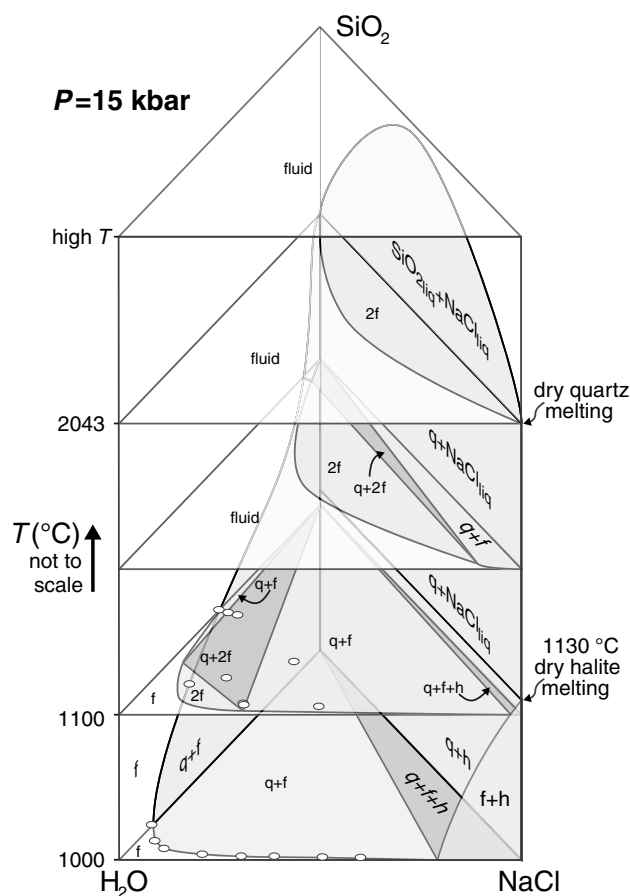

Fig. 8 Perspective view of semi-schematic isobaric 15 kbar ternary phase diagrams at progressively increasing temperature (vertical axis). Temperatures are selected to illustrate key changes in phase relations as halite melting and dry quartz melting boundaries are crossed. Fields with a single fluid phase are *white*, fields with two coexisting phases are *shaded light gray*, and those with three coexisting phases are *dark gray*. *Symbols* show data from this work, Hunt and Manning (2012; $X_{NaCl} = 0$, 1000 °C), and Nakamura (1974; $X_{NaCl} = 0$, 1100 °C). Dry melting of quartz taken from average of values of Hudon et al. (2002). Halite saturation and melting derived by linear extrapolation of results of Koster van Groos (1991)

Manning 2016). Any SiO_2–NaCl complexing could change the relative abundance of species inferred in our model.

Ternary phase relations

Effect of NaCl on critical mixing

Previous work indicates that, at 1100 °C and 12.5–15 kbar, the NaCl-free SiO_2–H_2O system lies at P and T higher than the upper critical end point on the hydrous melting curve of quartz, and is therefore supercritical with respect to melt–vapor mixing. However, results of the present study show that addition of only a small amount of NaCl leads to unmixing into two fluid phases, a siliceous fluid and a
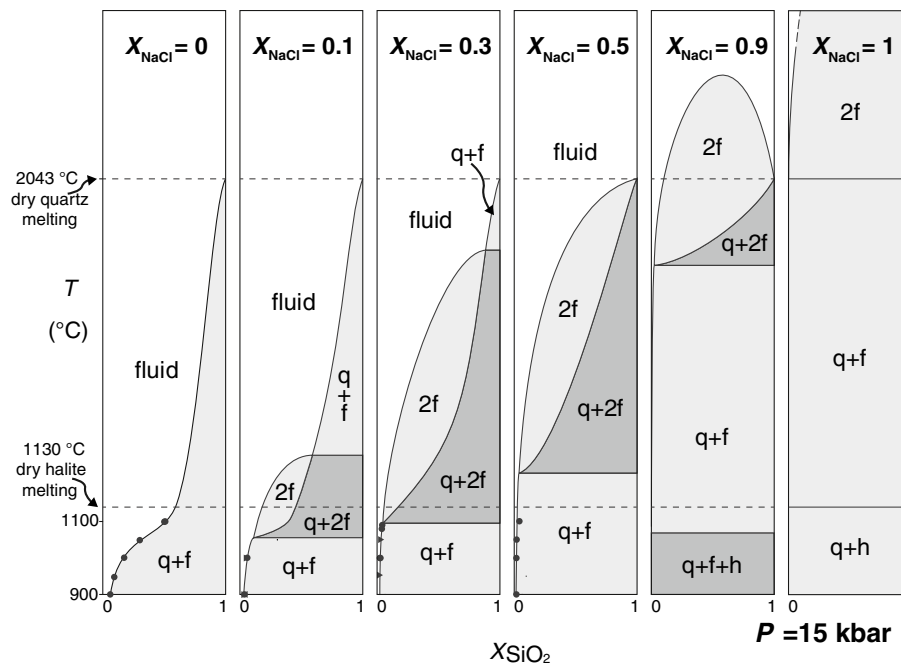
Fig. 9 Semi-schematic isobaric T–X pseudobinaries at various X_{NaCl} (15 kbar) showing the evolution from the supercritical SiO_2–H_2O system ($X_{NaCl} = 0$) to the subcritical SiO_2–NaCl system ($X_{NaCl} = 1$). Fields with a single fluid phase are *white*, fields with two coexisting phases are *shaded light gray*, and those with three coexisting phases are *dark gray*. *Markers* indicate where data constrain the interpretations; phase relations are otherwise approximate. *Circles* show the bulk compositions of experiments constraining the solubilities and phase boundaries. *Right- and left-pointing triangles* represent minimum and maximum solubilities, respectively. *Horizontal dashed lines* show dry melting of SiO_2 quartz from the average of the range of values of Hudon et al. (2002) and halite saturation and melting derived by linear extrapolation of results of Koster van Groos (1991)

saline fluid (Table 2; Fig. 5). Combining the solubility and phase-field data allows construction of a set of ternary diagrams, illustrating the evolution of phase relations with T above 1000 °C, at 15 kbar (Fig. 8). A SiO_2–H_2O fluid is supercritical at conditions of the diagrams, consistent with the location of the critical end point at 9.8 kbar (Kennedy et al. 1962; Newton and Manning 2008; Hunt and Manning 2012). The same is true for H_2O–NaCl fluids (Bowers and Helgeson 1983). Schematic phase relations along the SiO_2–NaCl face assume that when water is absent, SiO_2 and NaCl liquids are effectively immiscible to very high temperatures. Figure 8 conveys the changes in phase relations with temperature. The phase relations are consistent with our new data and previous results, but are otherwise largely schematic. At T lower than halite and quartz melting, the ternary consists solely of the solubility curve, which is the boundary between the quartz + fluid field and the fluid-only field. At T slightly below 1100 °C, the fluid separates into two phases yielding three two-phase fields and one three-phase field in which quartz stably coexists with two fluids. As T rises to 1100 °C, this field expands to include bulk compositions with $X_{NaCl} \sim 0.3$. Where two fluids are present, one is constrained to be H_2O–SiO_2 rich, consistent with electron microprobe analysis of quench glasses. The

other fluid must be NaCl rich but contain a minor amount of dissolved SiO_2, consistent with its production of quench roe rather than glass. The three additional two-phase fields are: two fluids, quartz + siliceous fluid, and quartz + saline fluid (Figs. 5, 8). As T rises further, the three- and two-phase fields migrate toward the SiO_2–NaCl join and the one-fluid field expands. When the T of dry melting of quartz is reached (~2043 °C; Hudon et al. 2002), the three-phase field disappears leaving only the two-fluid miscibility gap. Eventually, at some very high T, a single supercritical, completely miscible fluid is the only stable ternary phase.

Figure 9 depicts a series of isobaric pseudobinary diagrams at 15 kbar and various X_{NaCl}. At $X_{NaCl} = 0$, a SiO_2–H_2O fluid is supercritical, so a single solubility curve defines two stability fields, one for quartz + fluid and one for a single supercritical fluid. Between X_{NaCl} of 0 and 0.1, the ternary fluid phase separates. At all higher X_{NaCl}, a single fluid is stable at low X_{SiO_2}, a two-fluid field appears and grows larger with rising X_{NaCl}, and phase relations at high X_{SiO_2} vary from quartz + siliceous fluid at T below fluid unmixing, to quartz + saline fluid at higher T. Note that this saline fluid coexists with a second, more siliceous fluid over a finite T interval, above which a single fluid is again stable.

Fluid–fluid partitioning of Na and Cl

Where two fluid phases are inferred, electron microprobe and quench pH evidence supports the interpretation that Na partitions into the siliceous fluid and Cl partitions into the saline fluid. Hence, although we treat the system as ternary, once unmixing occurs it is strictly slightly quaternary, such that the siliceous fluid has a small Na excess and the saline fluid a small Cl excess.

Differential partitioning of Na and Cl between the two fluids is consistent with observations and experiments by other workers at lower pressures and temperatures, and in more compositionally complex systems. Numerous studies have demonstrated strong partitioning of Cl and other halogens into an aqueous fluid and incompatibility with the silicate melt at $P < 8$ kbar, and $T = 700$–1000 °C (Webster and Holloway 1988; Shinohara et al. 1989; Metrich and Rutherford 1992; Webster 1992; Kravchuk and Keppler 1994; Shinohara 1994; Candela and Piccoli 1995; Webster 1997; Webster and Rebbert 1998; Signorelli and Carroll 2000; Carroll 2005; Chevychelov et al. 2008; Alletti et al. 2009; Aranovich et al. 2013). Results from these investigations show that Cl partitioning varies with pressure, composition, particularly the overall Cl concentration of the system, and temperature to a lesser extent. Our preliminary results demonstrate that differential partitioning of Na and Cl persists to at least 15 kbar and 1100 °C for silicate melts in equilibrium with aqueous fluids. Nevertheless, the extent of the differential partitioning is relatively minor and is unlikely to strongly affect the topologies illustrated in Figs. 5, 8, and 9.

Solubility, polymerization, and critical mixing

The polymerization of silica in H_2O causes quartz solubility to increase much more extensively with T than it would were monomers the only solute (Newton and Manning 2002, 2003, 2008). This behavior leads to critical mixing of liquid + vapor at relatively low, geologically accessible P and T (Manning 2004; Newton and Manning 2008; Hunt and Manning 2012). Therefore, it should be expected that addition of a depolymerizing solute will also cause the upper critical end point to migrate to higher P (and T) and the ternary fluid to unmix at conditions where a SiO_2–H_2O fluid is otherwise supercritical. We find that this expectation holds in the investigated SiO_2–H_2O–NaCl system. Figure 7 shows that at 1000 °C, 15 kbar, addition of NaCl causes significant depolymerization of the dissolved silica. Trimers decrease from >50 % of silica to none as X_{NaCl} increases from 0 to 0.23, and the fraction of dimers decreases progressively as X_{NaCl} rises further. Similar relations must hold at 1100 °C, where rising X_{NaCl} also leads to fluid unmixing.

Our observations in the SiO_2–H_2O–NaCl system encourage a reinspection of phase relations in the system SiO_2–H_2O–CO_2. Newton and Manning (2009) revealed depolymerization of dissolved silica with increasing CO_2 mole fraction, similar to our results. In addition, Boettcher (1984) showed that the upper critical end point shifts from 9.8 to 19 kbar as X_{CO_2} increases from 0 to 0.05. Higher X_{CO_2} require the end point to lie at >25 kbar. Thus, although the solubility and melting data in the two studies were collected at very different P–T conditions, there is again a correlation between polymerization and critical mixing.

Thus it can be concluded that SiO_2 polymerization equilibria in the liquid, aqueous fluid, or supercritical phase control the location of critical mixing in the SiO_2–H_2O system. This is significant because, to the extent that SiO_2 is the major oxide in a wide range of crustal- and mantle-derived melts, it indicates that addition of NaCl, CO_2, or other depolymerizing agents decreases the stability range of multicomponent supercritical fluids.

Conclusions

1. At a fixed P and T, quartz solubility decreases with increasing X_{NaCl}. The strongest solubility declines are observed at the lowest X_{NaCl}. At all X_{NaCl}, solubility rises with T at constant P.
2. The dependence of quartz solubility on X_{NaCl} differs from that found by Newton and Manning (2000) at lower P and T, due to the substantially higher quartz solubilities in the present study.
3. High quartz solubilities can be explained by the presence of silica oligomers in addition to the monomers and dimers found at lower P and T. Modeling of results from 1000 °C, 15 kbar, in which these species are assumed to be trimers, implies that they contain >50 % of dissolved Si in quartz-saturated SiO_2–H_2O, that their abundance decreases with increasing X_{NaCl}, and that they become negligible at $X_{NaCl} = 0.23$.
4. Fluid in the system SiO_2–H_2O is supercritical at all conditions of the present study; however, addition of only a small amount of NaCl causes unmixing to two fluid phases. At 1100 °C, 15 kbar, evidence for two fluids was observed at $X_{NaCl} = 0.05$ and results indicate the two-fluid field extends at least $X_{NaCl} = 0.3$.
5. Increasing X_{NaCl} at 1000 °C, 15 kbar, leads to depolymerization, as measured by the OH/Si ratio. At 1100 °C, increasing X_{NaCl} causes fluid unmixing. This correspondence supports the hypothesis that critical mixing between silicate liquids and H_2O-rich fluids is promoted by polymerization of rock-forming components, especially SiO_2 (Manning 2004; Newton and Manning 2008; Hunt and Manning 2012), and that addition of

depolymerizing agents decreases the *P–T* stability of supercritical multicomponent fluids.

References

Alletti M, Baker DR, Scaillet B et al (2009) Chlorine partitioning between a basaltic melt and H_2O–CO_2 fluids at Mount Etna. Chem Geol 263:37–50

Anderson GM, Burnham CW (1965) The solubility of quartz in supercritical water. Am J Sci 263:494–511

Antignano A, Manning CE (2008a) Fluorapatite solubility in H_2O and H_2O–NaCl at 700 to 900 °C and 0.7 to 2.0 GPa. Chem Geol 251:112–119

Antignano A, Manning CE (2008b) Rutile solubility in H_2O, H_2O–SiO_2, and H_2O–$NaAlSi_3O_8$ fluids at 0.7–2.0 GPa and 700–1000 °C: implications for mobility of nominally insoluble elements. Chem Geol 255:283–293

Aranovich LY, Newton RC (1996) H_2O activity in concentrated NaCl solutions at high pressures and temperatures measured by the brucite–periclase equilibrium. Contrib Mineral Petrol 125:200–212

Aranovich LY, Newton RC, Manning CE (2013) Brine-assisted anatexis: experimental melting in the system haplogranite–H_2O–NaCl–KCl at deep-crustal conditions. Earth Planet Sci Lett 374:111–120

Boettcher AL (1984) The system SiO_2–H_2O–CO_2; melting, solubility mechanisms of carbon, and liquid structure to high pressures. Am Mineral 69:823–833

Bowers T, Helgeson H (1983) Calculation of the thermodynamic and geochemical consequences of nonideal mixing in the system H_2O–CO_2–NaCl on phase relations in geologic systems. Geochim Cosmochim Acta 47:1247–1275

Bureau H, Keppler H (1999) Complete miscibility between silicate melts and hydrous fluids in the upper mantle: experimental evidence and geochemical implications. Earth Planet Sci Lett 165:187–196

Caciagli NC, Manning CE (2003) The solubility of calcite in water at 6–16 kbar and 500–800 °C. Contrib Mineral Petrol 146:275–285

Candela PA, Piccoli PM (1995) An experimental–theoretical model of brine-vapor-silicate melt equilibria with applications to geothermal and ore-forming systems. Magmas Fluids Ore Depos 23:101–127

Carroll MR (2005) Chlorine solubility in evolved alkaline magmas. Ann Geophys 48:619–631

Cheng VM, Allen PG, Lazarus D (1975) Pressure coefficient of thermoelectric power of platinum/platinum – 10 % rhodium and chromel/alumel thermocouples. Appl Phys Lett 26:6–7

Chevychelov VY, Botcharnikov RE, Holtz F (2008) Partitioning of Cl and F between fluid and hydrous phonolitic melt of Mt. Vesuvius at ~850–1000 °C and 200 MPa. Chem Geol 256:172–184

Evans K (2007) Quartz solubility in salt-bearing solutions at pressures to 1 GPa and temperatures to 900 °C. Geofluids 7:451–467

Gerya TV, Maresch WV, Burchard M et al (2005) Thermodynamic modeling of solubility and speciation of silica in H_2O–SiO_2 fluid up to 1300 °C and 20 kbar based on the chain reaction formalism. Eur J Mineral 17:269–283

Getting IC, Kennedy GC (1970) Effect of pressure on the emf of chromel–alumel and platinum–platinum 10 % rhodium thermocouples. J Appl Phys 41:4552–4562

Hack AC, Hermann J, Mavrogenes JA (2007a) Mineral solubility and hydrous melting relations in the deep earth: analysis of some binary A-H_2O system pressure–temperature–composition topologies. Am J Sci 307:833–855

Hack AC, Thompson AB, Aerts M (2007b) Phase relations involving hydrous silicate melts, aqueous fluids, and minerals. Rev Mineral Geochem 65:129–185

Hermann J, Spandler CJ (2008) Sediment melts at sub-arc depths: an experimental study. J Petrol 49: 717–740

Hermann J, Spandler C, Hack A, Korsakov A (2006) Aqueous fluids and hydrous melts in high-pressure and ultra-high pressure rocks: implications for element transfer in subduction zones. Lithos 92:399–417

Hermann J, Zheng Y-F, Rubatto D (2013) Deep fluids in subducted continental crust. Elements 9:281–287

Hudon P, Jung I, Baker D (2002) Melting of [beta]-quartz up to 2.0 GPa and thermodynamic optimization of the silica liquidus up to 6.0 GPa. Phys Earth Planet Inter 130:159–174

Hunt JD, Manning CE (2012) A thermodynamic model for the system near the upper critical end point based on quartz solubility experiments at 500–1100 °C and 5–20 kbar. Geochim Cosmochim Acta 86:196–213

Jackson I (1976) Melting of the silica isotypes SiO_2, BeF_2 and GeO_2 at elevated pressures. Phys Earth Planet Inter 13:218–231

Kawamoto T, Kanzaki M, Mibe K et al (2012) Separation of supercritical slab-fluids to form aqueous fluid and melt components in subduction zone magmatism. Proc Natl Acad Sci 109:18695–18700

Kennedy GC, Wasserburg GJ, Heard HC, Newton RC (1962) The upper three-phase region in the system SiO_2–H_2O. Am J Sci 260:501–521

Keppler H (1996) Constraints from partitioning experiments on the composition of subduction-zone fluids. Nature 380:237–240

Koster van Groos AF (1991) Differential thermal analysis of the liquidus relations in the system NaCl–H_2O to 6 kbar. Geochim Cosmochim Acta 55:2811–2817

Kravchuk IF, Keppler H (1994) Distribution of chloride between aqueous fluids and felsic melts at 2 kbar and 800 °C. Eur J Mineral 6:913–923

Manning CE (1994) The solubility of quartz in H_2O in the lower crust and upper mantle. Geochim Cosmochim Acta 58:4831–4839

Manning CE (2004) The chemistry of subduction-zone fluids. Earth Planet Sci Lett 223:1–16

Manning CE, Aranovich LY (2014) Brines at high pressure and temperature: thermodynamic, petrologic and geochemical effects. Precambr Res 253:6–16

Manning CE, Boettcher SL (1994) Rapid-quench hydrothermal experiments at mantle pressures and temperatures. Am Mineral 79:1153–1158

Metrich N, Rutherford MJ (1992) Experimental study of chlorine behavior in hydrous silicic melts. Geochim Cosmochim Acta 56:607–616

Mibe K, Kanzaki M, Kawamoto T et al (2004) Determination of the second critical end point in silicate–H_2O systems using high-pressure and high-temperature X-ray radiography. Geochim Cosmochim Acta 68:5189–5195

Mibe K, Kanzaki M, Kawamoto T et al (2007) Second critical end-point in the peridotite–H_2O system. J Geophys Res 112:B03201

Mibe K, Kawamoto T, Matsukage KN et al (2011) Slab melting versus slab dehydration in subduction-zone magmatism. PNAS 108:8177–8182

Mysen BO (1988) Structure and properties of silicate melts. Elsevier, Amsterdam

Mysen BO (2010) Speciation and mixing behavior of silica-saturated aqueous fluid at high temperature and pressure. Am Mineral 95:1807–1816

Mysen BO, Richet P (2005) Silicate glasses and melts: properties and structure, vol 10. Elsevier, Amsterdam

Mysen BO, Mibe K, Chou IM, Bassett W (2013) Structure and equilibria among silicate species in aqueous fluids in the upper mantle: experimental SiO_2–H_2O and MgO–SiO_2–H_2O data recorded in situ to 900 °C and 5.4 GPa. J Geophys Res Solid Earth 118:6076–6085

Nakamura Y (1974) The system SiO_2–H_2O–H_2 at 15 kbar. Carnegie Inst Wash Yearbook 73:259–263

Newton RC, Manning CE (2000) Quartz solubility in H_2O–NaCl and H_2O–CO_2 solutions at deep crust-upper mantle pressures and temperatures: 2–15 kbar and 500–900°C. Geochim Cosmochim Acta 64:2993–3005

Newton RC, Manning CE (2002) Solubility of enstatite + forsterite in H_2O at deep crust/upper mantle conditions: 4 to 15 kbar and 700 to 900°C. Geochim Cosmochim Acta 66:4165–4176

Newton RC, Manning CE (2003) Activity coefficient and polymerization of aqueous silica at 800 °C, 12 kbar, from solubility measurements on SiO_2-buffering mineral assemblages. Contrib Mineral Petrol 146:135–143

Newton RC, Manning CE (2006) Solubilities of corundum, wollastonite and quartz in H_2O–NaCl solutions at 800 °C and 10 kbar: interaction of simple minerals with brines at high pressure and temperature. Geochim Cosmochim Acta 70:5571–5582

Newton RC, Manning CE (2008) Thermodynamics of SiO_2–H_2O fluid near the upper critical end point from quartz solubility measurements at 10 kbar. Earth Planet Sci Lett 274:241–249

Newton RC, Manning CE (2009) Hydration state and activity of aqueous silica in H_2O–CO_2 fluids at high pressure and temperature. Am Mineral 94:1287–1290

Newton RC, Manning CE (2010) Role of saline fluids in deep-crustal and upper-mantle metasomatism: insights from experimental studies. Geofluids 10:58–72

Newton RC, Manning CE (2016) Evidence for SiO_2–NaCl complexing in H_2O–NaCl solutions at high pressure and temperature. Geofluids. doi:10.1111/gfl.12153

Newton RC, Aranovich LY, Hansen EC, Vandenheuvel BA (1998) Hypersaline fluids in Precambrian deep-crustal metamorphism. Precamb Res 91:41–63

Novgorodov PG (1977) On the solubility of quartz in H_2O + CO_2 and H_2O + NaCl at 700 °C and 1.5 kb pressure. Geochem Int 14:191–193

Paillat O, Elphick SC, Brown WL (1992) The solubility of water in $NaAlSi_3O_8$ melts: a re-examination of Ab − H_2O phase relationships and critical behaviour at high pressures. Contrib Mineral Petrol 112:490–500

Shen A, Keppler H (1997) Direct observation of complete miscibility in the albite–H_2O system. Nature 385:710–712

Shinohara H (1994) Exsolution of immiscible vapor and liquid phases from a crystallizing silicate melt: implications for chlorine and metal transport. Geochim Cosmochim Acta 58:5215–5221

Shinohara H, Iiyama JT, Matsuo S (1989) Partition of chlorine compounds between silicate melt and hydrothermal solutions: I. Partition of NaCl–KCl. Geochim Cosmochim Acta 53:2617–2630

Shmulovich KI, Graham CM (2004) An experimental study of phase equilibria in the systems H_2O–CO_2–CaCl2 and H_2O–CO_2–NaCl at high pressures and temperatures (500–800 °C, 0.5–0.9 GPa): geological and geophysical applications. Contrib Mineral Petrol 146:450–462

Shmulovich K, Graham C, Yardley B (2001) Quartz, albite and diopside solubilities in H_2O–NaCl and H_2O–CO_2 fluids at 0.5–0.9 GPa. Contrib Mineral Petrol 141:95–108

Shmulovich KI, Yardley B, Graham CM (2006) Solubility of quartz in crustal fluids: experiments and general equations for salt solutions and H_2O–CO_2 mixtures at 400–800 °C and 0.1–0.9 GPa. Geofluids 6:154–167

Signorelli S, Carroll MR (2000) Solubility and fluid-melt partitioning of Cl in hydrous phonolitic melts. Geochim Cosmochim Acta 64:2851–2862

Stalder R, Ulmer P, Thompson AB, Günther D (2000) Experimental approach to constrain second critical end points in fluid/silicate systems: near-solidus fluids and melts in the system albite–H_2O. Am Mineral 85:68–77

Stalder R, Ulmer P, Thompson A, Günther D (2001) High pressure fluids in the system MgO–SiO_2–H_2O under upper mantle conditions. Contrib Mineral Petrol 140:607–618

Stebbins JF (1988) Effects of temperature and composition on silicate glass structure and dynamics: Si-29 NMR results. J Non-Cryst Solids 106(1):359–369

Stebbins JF (1995) Dynamics and structure of silicate and oxide melts; nuclear magnetic resonance studies. Rev Mineral Geochem 32(1):191–246

Touret JLR (1985) Fluid regime in southern Norway: the record of fluid inclusions. In: Tobi AC, Touret JLR (eds) The deep proterozoic crust in the North Atlantic Provinces. Springer, Dordrecht, pp 517–549

Tropper P, Manning CE (2005) Very low solubility of rutile in H_2O at high pressure and temperature, and its implications for Ti mobility in subduction zones. Am Mineral 90:502–505

Walther JV, Orville PM (1983) The extraction–quench technique for determination of the thermodynamic properties of solute complexes: application to quartz solubility in fluid mixtures. Am Mineral 68:731–741

Webster JD (1992) Water solubility and chlorine partitioning in Cl-rich granitic systems: effects of melt composition at 2 kbar and 800°C. Geochim Cosmochim Acta 56:679–687

Webster JD (1997) Chloride solubility in felsic melts and the role of chloride in magmatic degassing. J Petrol 38:1793–1807

Webster JD, Holloway JR (1988) Experimental constraints on the partitioning of Cl between topaz rhyolite melt and H_2O and H_2O + CO_2 fluids: new implications for granitic differentiation and ore deposition. Geochim Cosmochim Acta 52:2091–2105

Webster JD, Rebbert CR (1998) Experimental investigation of H_2O and Cl^- solubilities in F-enriched silicate liquids; implications for volatile saturation of topaz rhyolite magmas. Contrib Mineral Petrol 132:198–207

Xie Z, Walther JV (1993) Quartz solubilities in NaCl solutions with and without wollastonite at elevated temperatures and pressures. Geochim Cosmochim Acta 57:1947–1955

Zhang Y-G, Frantz JD (2000) Enstatite–forsterite–water equilibria at elevated temperatures and pressures. Am Mineral 85:918–925

Zheng Y-F, Xia Q-X, Chen R-X, Gao X-Y (2011) Partial melting, fluid supercriticality and element mobility in ultrahigh-pressure metamorphic rocks during continental collision. Earth-Sci Rev 107:342–374

Zotov N, Keppler H (2000) In-situ Raman spectra of dissolved silica species in aqueous fluids to 900 °C and 14 kbar. Am Mineral 85:600–603

Zotov N, Keppler H (2002) Silica speciation in aqueous fluids at high pressures and high temperatures. Chem Geol 184:71–82